scientific reports

Check for updates

OPEN

Stacking ensemble machine learning for predicting photodetector performance under varying illumination intensities

Ali Öter[1,2], Zeynep Berktaş[3], Betül Ersöz[4], Şeref Sağıroğlu[5,7]✉ & Elif Orhan[6,7]✉

Photodetectors are essential components in modern optoelectronic technologies, yet experimental characterization of nanomaterial-based devices is often time-consuming and resource-intensive. To address this challenge, this study presents a stacking ensemble learning approach to predict the performance of bismuth-doped graphene quantum dots-based photodetectors under illumination levels ranging from 22 to 110 mW/mm². Four boosting algorithms—Adaptive Boosting, Gradient Boosting, Extreme Gradient Boosting, and Categorical Boosting—were trained on datasets obtained under dark, 22, 66, and 110 mW/mm², while 44 and 88 mW/mm² data were reserved for testing. A stacking ensemble learning model further enhanced prediction accuracy. The final model achieved a coefficient of determination of 0.9874 and a mean absolute error of 0.1840 at 88 mW/mm², effectively predicting the logarithmic current–voltage characteristics. The model also estimated key photodetector metrics, including sensitivity (1589.27), responsivity (2.389 mA/W), and specific detectivity (1.16×10^{10} Jones). This study explores the use of a stacking ensemble of four boosting algorithms to model the performance of Bi-GQD/p-Si photodetectors across different illumination levels, offering a data-driven alternative to traditional characterization.

Keywords Ensemble learning, Machine learning, Stacking, Boosting algorithms, Illumination intensity, Photodetector performance

Photodetectors play a critical role in a wide range of applications, including optical communication, imaging, and environmental sensing. Among emerging materials, graphene quantum dots (GQDs) doped with various elements have attracted significant attention due to their unique optoelectronic properties. Studies have shown that incorporating GQDs into photodetectors can significantly enhance their performance[1–3]. GQDs have been shown to enhance the performance of various photodetectors, including those based on MoS_2 and perovskite materials, achieving high photoresponsivity and photogain[4,5]. A GQDs/perovskite bilayer heterostructure photodetector exhibited improved on/off ratio and photoresponsivity compared to single-layer devices[5]. Similarly, GQDs sandwiched between graphene sheets demonstrated high detectivity and responsivity across a broad spectral range[6]. In this context, bismuth-doped graphene quantum dots (Bi-GQDs) were selected as the active material in this study. While halide perovskite QDs (HPQDs) have shown outstanding optoelectronic performance, including nearly unity PLQY and tunable bandgaps[7–9], their practical use is limited by poor stability under light, heat, and moisture, as well as lead toxicity[10]. In contrast, Bi-based QD systems offer enhanced chemical stability, environmental safety, and reproducibility. Moreover, Bi doping has been shown to effectively modulate band structures and carrier dynamics[11–13]. Thus, Bi-GQDs offer a stable and reproducible platform, making them a suitable choice for this proof-of-concept study.

Traditional experimental methods to characterize photodetector performance are often time-consuming and resource-intensive. However, accurately predicting the electrical and photophysical characteristics of such advanced photodetectors under varying illumination conditions remains a challenge. Recently, machine learning (ML) techniques have emerged as powerful tools for accelerating device modeling and reducing experimental

[1]Department of Electronics and Automation, Kahramanmaraş Sütçü İmam University, Kahramanmaraş 46030, Turkey. [2]Department of Energy Systems Engineering, Gazi University, Ankara 06500, Turkey. [3]Electrical-Electronics Engineering, Ankara Medipol University, Ankara 06050, Turkey. [4]Department of Computer and Instructional Technologies Education, Gazi University, Ankara 06500, Turkey. [5]Department of Computer Engineering, Gazi University, Ankara 06500, Turkey. [6]Department of Physics, Gazi University, Ankara 06500, Turkey. [7]Şeref Sağıroğlu and Elif Orhan contributed equally to this work. ✉email: ss@gazi.edu.tr; eliforhan@gazi.edu.tr

load[14,15]. Among these, ensemble methods in ML techniques combine various classifiers to improve predictive performance and accuracy compared to single models used in modelling[16,17]. Popular ensemble techniques include boosting, bagging, and stacking[17,18] to be used for complex problem-solving to extend various domains, including face recognition, object tracking, and bioinformatics making it a powerful tool for[19], energy forecasting[20], medical image analyzing[21], and educational data mining[22]. Despite their success in fields such as their application to photodetector characterization remains limited.

The key to photodetector performance lies in attaining high responsivity and detectivity, which has driven extensive research efforts in device design. The ML models achieved high accuracy (> 94%) in predicting photodetector performance metrics[23]. Pandey et al.[24] modeled responsivity and detectivity in two-dimensional metal halide perovskite photodetectors using six predictors, including a decision tree (DT)-based model with incident light intensity as a feature, achieving low root mean square errors of 0.0092 for responsivity and 0.0695 for detectivity, along with validation errors of 1.09×10^{-2} and 7.41×10^{-6}, respectively. In designing near-IR organic semiconductors for photodetectors, Extra Trees and Random Forest (RF) algorithms outperformed in comparison with other algorithms in predicting material properties[25]. For photovoltaic systems, RF algorithm exhibited superior performance over AdaBoost in predicting output current, with a lower mean absolute error of 0.27% compared to AdaBoost's 34.5%[26]. These studies highlight the effectiveness of ensemble ML methods in accurately predicting various photodetector characteristics, potentially accelerating the development and optimization of photodetector technologies. Ensemble ML methods—particularly CatBoost—have demonstrated strong capability in accurately predicting the maximum photovoltaic current under varying illumination conditions[27] and high-performance devices[28]. Iborra et al.[29] used an ensemble ML model for monolithic positron emission tomography detectors, achieving full width at half maximum between 2 and 2.4 mm and improvements in signal-to-noise, contrast-to-noise, and structural similarity metrics. Employing an ensemble of multilayer perceptron neural networks (MLPNNs) in monolithic positron emission tomography detectors, obtaining full width at half maximum values between 2 and 2.4 mm and describing improvements in signal-to-noise, contrast-to-noise, and structural similarity metrics. Sorathiya et al.[30] focused on graphene-based field-effect transistor photodetectors under deep ultraviolet illumination, demonstrating that polynomial regression surpassed linear regression as measured by the coefficient of determination and mean square error. These studies indicate that while individual supervised learning models yield accurate predictions under specified conditions, ensemble methods—as used by Iborra et al.[29]—offer enhanced generalizability across diverse detector designs.

Limited and varied reporting of illumination conditions precludes a comprehensive comparison across approaches, yet the inclusion of incident light intensity[24] and targeted illumination regimes[30] provides some evidence of handling variable illumination in photodetector characterization. While most previous studies compared individual models and selected the best-performing one—such as DT -based or polynomial regression models—only Iborra et al.[29] explicitly employed an ensemble machine learning approach, utilizing an ensemble of MLPNNs.

In addition to machine learning-based prediction studies, significant progress has also been made in the field of reconfigurable and spectrally tunable photodetectors. Early demonstrations include graphene-based wavelength-tunable devices[31] and electrically tunable photoresponse in nanostructured systems[32]. More recent works have introduced advanced reconfigurable architectures[33] and novel material-based tuning mechanisms[34]. While these pioneering studies focus primarily on spectral tunability, our approach addresses the complementary challenge of intensity-dependent performance prediction by applying ensemble machine learning to Bi-doped GQDs photodetectors.

Building on this gap, we present a practical and accurate method for predicting photodetector behavior under varying illumination levels using ensemble ML techniques, offering enhanced generalizability and prediction performance compared to single-model approaches. Models were trained using experimental semilogarithmic current–voltage ($ln(I)$–V) data obtained from a bismuth (Bi)-doped GQDs-based photodetector operating under illumination levels ranging from 22, 66, and 110 mW/mm² for training and intermediate levels (44 and 88 mW/mm²) for test. The results show that the models can reliably estimate ln(I)–V characteristics as well as key performance metrics such as responsivity and detectivity, even at unseen illumination levels. By leveraging a limited set of experimental data and advanced ML techniques, our method aims to reduce experimental workload while providing reliable predictions across varying illumination conditions, thus offering a powerful tool for rapid photodetector design and optimization.

This study introduces a stacking ensemble framework combining four boosting algorithms (AdaBoost, Gradient Boosting, XGBoost, and CatBoost) to predict the performance of Bi-doped GQDs/p-Si photodetectors under multiple illumination levels, providing a data-driven and efficient alternative to traditional experimental characterization.

Materials and methods

Ensemble learning boosting algorithms have demonstrated strong performance across various ML applications[35]. These algorithms improve prediction accuracy and generalization by combining multiple base learners into a single, more robust model[36].

In this study, a nanocomposite diode based on Bi-GQDs/p-Si was fabricated. First, GQDs were synthesized using a green hydrothermal method. A solution of $BiO(NO_3)$ was then introduced into the GQDs matrix. The resulting nanocomposite was spin-coated onto a p-type silicon (100) wafer (resistivity: 1–10 Ω·cm, thickness: 350 μm), forming a thin film approximately 30 nm thick. Gold (Au) contacts were deposited using a sputtering technique. Further fabrication details are provided in[1,2]. The schematic configuration of the fabricated Bi-GQDs/p-Si photodetector is illustrated in Fig. 1. Nine diodes were fabricated on one-quarter of a 4-inch wafer under identical deposition and annealing conditions. The I–V characteristics of all devices were analyzed using a custom Python script that automatically extracts key parameters—including ideality factor, barrier height, and

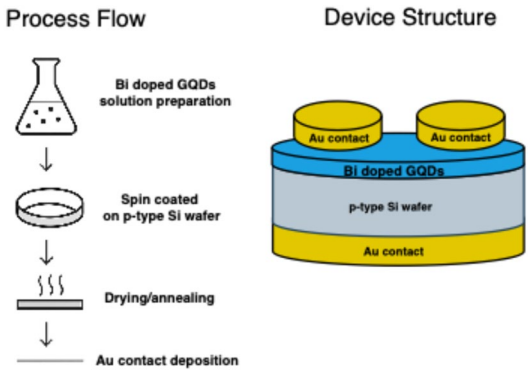


Fig. 1. Schematic diagram of the fabricated Bi-GQDs/p-Si photodetector structure. The device consists of a 125 nm Au top contact, a spin-coated Bi-GQDs layer on a p-type Si substrate, and a 100 nm Au back contact.

Device ID	Structure	Active Area (mm^2)	Bias range (V)	Illumination levels (mW/mm^2)	Notes
D1	Bi-GQDs/p-Si device	0.785	−5 to + 5	Dark, 22, 44, 66, 88, 110	Single proof-of-concept device, measured at 300 K

Table 1. Summary of the fabricated Bi-GQDs/p-Si photodetector, showing its structural configuration, active area, applied bias range, illumination levels, and experimental measurement conditions at 300 K.

Illumination levels (mW/mm^2)	Role in ML dataset	Voltage step size (V)	Data points per level	Measurement conditions
Dark	Training	0.01	1000	300 K, Keithley 4200 SCS
22	Training	0.01	1000	300 K, Keithley 4200 SCS
44	Testing	0.01	1000	300 K, Keithley 4200 SCS
66	Training	0.01	1000	300 K, Keithley 4200 SCS
88	Testing	0.01	1000	300 K, Keithley 4200 SCS
110	Training	0.01	1000	300 K, Keithley 4200 SCS

Table 2. Dataset description used for ML analysis, showing the illumination levels, roles in training/testing, voltage step size, and measurement conditions.

rectification ratio—and determines the most stable diode for ML modeling. This automated selection procedure, validated in our previous open-access work[15], ensures objective and reproducible identification based on quantitative electrical metrics.

The electrical and photodetection measurements were performed using a source-measure unit (Keithley 4200 SCS) under both dark and illuminated conditions. For illumination, a supercontinuum light source (SuperK Compact, NKT Photonics) with a spectral range of 450–2400 nm was employed. The output intensity of the white light was controlled using a calibrated power controller, and the incident power density was varied from 22 to 110 $mW{\cdot}mm^2$. The current–voltage (I–V) characteristics were systematically examined under these conditions. Only one Bi-GQDs/p-Si photodetector was fabricated for this proof-of-concept study. Measurements were performed under controlled illumination conditions at room temperature. The device details and testing parameters are summarized in Table 1.

To model the diode's nonlinear photoresponse behavior, four advanced boosting algorithms—AdaBoost, Gradient Boosting (GB), XGBoost, and CatBoost—were trained and evaluated. Finally, their outputs were trained again using a stacking ensemble method to further improve the prediction performance of the characteristics. Datasets obtained under dark, 22 mW/mm^2, 66 mW/mm^2, and 110 mW/mm^2 illumination were used for training, while data corresponding to 44 mW/mm^2 and 88 mW/mm^2 were reserved for testing. The datasets used for training and testing were derived from $ln(I)$–V measurements of the Bi-GQD/p-Si photodetector under six illumination conditions. Dark, 22, 66, and 110 mW/mm^2 levels were used for training, while 44 and 88 mW/mm^2 levels were reserved for testing. Table 2 summarizes the illumination levels, their respective roles in model training and testing, the applied voltage step size, the number of data points collected at each level, and the experimental measurement conditions. The dataset was acquired at 300 K using a Keithley 4200 SCS source-measurement unit with a voltage step size of 0.01 V, providing 1000 data points per illumination level for robust ML model development.

Models	Parameters used in trainings	Parameters of the best model
AdaBoost	n_estimator: 50, 100, 200 learning_rate: 0.01, 0.1, 1.0 estimator__loss: linear, square, exponential random_state:42	n_estimator: 100 learning_rate: 1.0 estimator__loss: square random_state:42
GB	n_estimator: 100, 200, 300 learning_rate: 0.01, 0.05, 0.1 max_depth: 3, 4, 5 min_samples_split: 2, 5, 10 random_state:42	n_estimator: 300 learning_rate: 0.1 max_depth: 5 min_samples_split: 10 random_state:42
XGB	n_estimator: 100, 200, 300 learning_rate: 0.01, 0.05, 0.1 max_depth: 3, 5, 7 subsample: 0.8, 1.0 random_state:42	n_estimator:200 learning_rate: 0.1 max_depth: 5 subsample: 1.0 random_state:42
CatBoost	n_estimator: 200, 500, 800 learning_rate: 0.01, 0.05, 0.1 max_depth: 4, 6, 8 random_state:42	n_estimator: 800 learning_rate: 0.5 max_depth: 8 random_state:42

Table 3. Hyperparameters of the AI models used in this study, including the parameter ranges explored during training and the optimized values for each model.

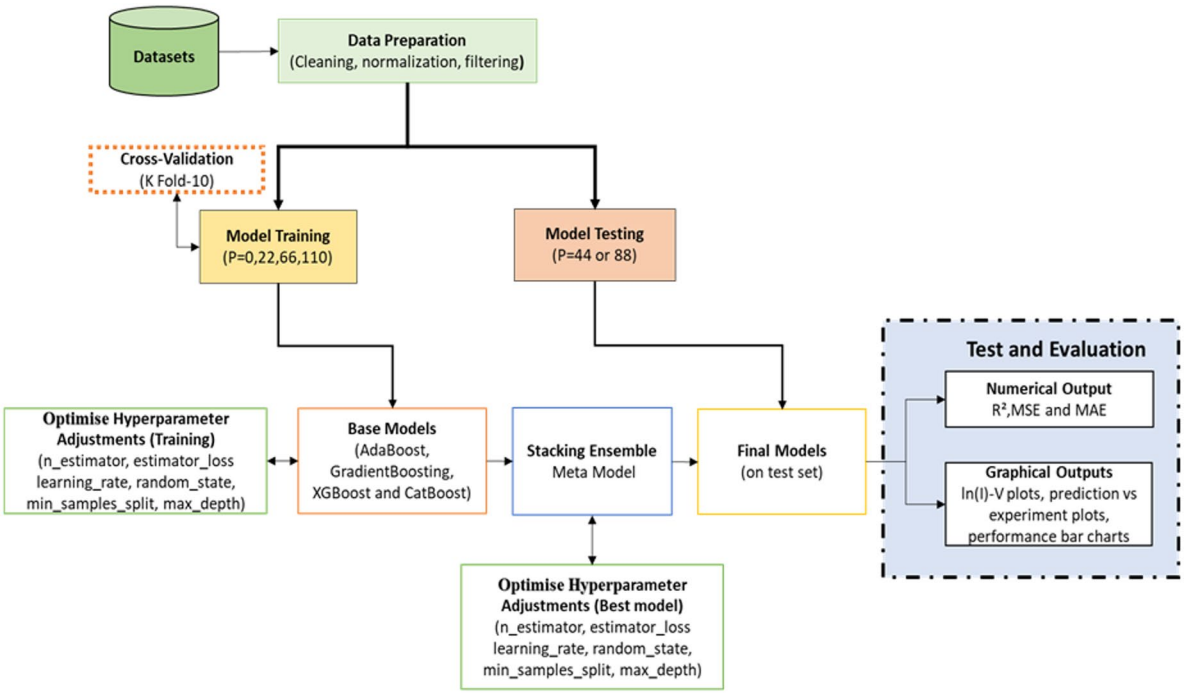


Fig. 2. Flowchart of the stacking ensemble model training and evaluation process. The workflow begins with dataset preparation, including cleaning, normalization, and filtering. K-fold cross-validation (K = 10) is applied to ensure generalization during model training.

Model performance was evaluated based on their ability to accurately reproduce the *ln(I)–V* characteristics of the test data. Table 3 summarizes both the parameter ranges explored during the training phase and the optimal hyperparameters obtained after grid-search optimization for each base learner. Four ensemble learning algorithms—AdaBoost, GB, XGBoost, and CatBoost—were tuned to achieve the best predictive performance of the stacking ensemble framework. The overall methodology is schematically illustrated in Fig. 2.

As can be seen from Fig. 2 and Table 2, this study employed four advanced boosting algorithms—AdaBoost, GB, XGBoost, and CatBoost to predict the illuminated dependent I-V characteristics of a Bi-GQDs/p-Si nanocomposite photodetector individually, and also combine the power of five models' predictions of the characteristics with the help of Stacking Ensemble Learning to improve the prediction of the characteristics better than each of individual models. These algorithms are briefly described below:

Adaptive Boosting (AdaBoost) is considered one of the first boosting algorithms by Ferreira and Figueiredo[37]It is an algorithm that performs mass learning in the field of ML and aims to combine weak learners and obtain a strong learner. In this algorithm, each weak learner is trained individually and works by giving weights according

to the performance of each model. The data learned incorrectly in the first prediction is trained by giving more priority in the training next step. As a result, more successful results are obtained by combining weak learners.

Gradient Boosting (GB) is an ensemble learning technique that builds a series of weak learners (typically DTs) iteratively. Each new tree tries to correct the errors made by the previous ones, making the final model a strong predictor.

The estimated value for a data point in the t-th iteration is given by:

$$\mathrm{F}_t\left(\mathrm{x}\right) = \mathrm{F}_{t-1}\left(\mathcal{X}\right) + \gamma\, \mathrm{h}_\mathrm{t}\left(\mathcal{X}\right) \tag{1}$$

where:

$F_t\left(x\right)$ t is the predicted value at iteration,

$\mathrm{F}_{t-1}\left(\mathcal{X}\right)$ is the predicted value from the previous iteration,

$\mathrm{h}_\mathrm{t}\left(\mathcal{X}\right)$ is the weak model (usually a DT) added at iteration **t**,

γ is the learning rate, controlling how much each weak model contributes to the final prediction.

eXtreme Gradient Boosting (XGBoost) was developed by Chen and Guestrin[38] and itis a supervised ML method based on the basic principles of GB algorithm. This algorithm consists of classification and regression DT approaches and aims to produce a strong learning algorithm by combining a large number of weak learning models. Weak learning models form regression trees, the success of the algorithm is calculated and the residual (error score) is used to form the next tree with the iteration method. As a result, the method used gives successful results in solving complex problems.

CatBoost is a fast, effective and practical ML library developed to analyze categorical data with a GB-based tree-based feature that does not require one-hot encoding or label encoding. Unlike other boosting algorithms, it has a minimal variance sampling technique. In the technique, weighted sampling is performed at the tree level rather than at the separation level. This prevents the overfitting problem in small data sets[39].

Stacking Ensemble Learning uses a variety of learning algorithms to develop its models, and then a combiner algorithm is trained to use the base algorithms' predictions to produce the final predictions. In stacking, the original data is fed into a variety of different models. The input and output of each model, together with the weights, are then estimated using the metaclassifier. The models that perform the best are selected, while the others are disqualified. A metaclassifier is used in stacking to combine several basic classifiers that were learned on a single dataset using various learning techniques. To create a fresh set of predictions, the inputs from each subsequent layer are combined with the model's predictions. A combiner algorithm is trained using the predictions produced by the base algorithms to provide the final predictions after stacking creates its models using various learning algorithms. Any ensemble approach can be used as this combiner[40,41].

Model performance metrics

The performance of the regression models was evaluated using four common statistical metrics: R-squared (R^2), Mean Squared Error (*MSE*), and Mean Absolute Error (*MAE*). These evaluation metrics help assess and improve the model's predictive power before applying it to new data.

R^2 indicates how well the model explains the variance in the data, with values closer to "1" representing better fit. *MSE* measures the average of the squared differences between predicted and actual values, where lower values indicate more accurate predictions. *MAE* calculates the average absolute difference between predictions and actual values, offering an intuitive measure of error magnitude. These metrics were chosen to comprehensively assess model accuracy, considering the magnitude and relative size of errors and the model's overall fit to the data. Below, the mathematical representations of the R^2, *MSE*, *and MAE* metrics are provided.

$$R^2 = 1 - \frac{\sum_i^N \left(Y_{predict(i)} - Y_i\right)^2}{\sum_i^N \left(Y_i - Y_{mean}\right)^2} \tag{2}$$

$$MSE = \frac{1}{N}\sum_i^N \left(Y_i - Y_{predict(i)}\right)^2 \tag{3}$$

$$MAE = \frac{1}{N}\sum_{i=1}^N \left|Y_{predict(i)} - Y_{mean}\right| \tag{4}$$

where:

Y_i : Actual value, $Y_{predict(i)}$: Value predicted by the model, Y_{mean}: Mean of the actual values, N: Number of data points.

Results and discussion

This study utilized *I–V* measurements obtained from a Bi-GQDs/p-Si nanocomposite device to train and evaluate four boosting algorithms—AdaBoost, GB, XGBoost, and CatBoost—for predicting the illumination-dependent *I–V* characteristics of the device. To further enhance predictive performance, a stacking ensemble approach was employed to combine the outputs of the individual models. For each illumination, 1000 *ln(I)–V* data points were collected, with the voltage (*V*) ranging from − 5 V to + 5 V in 0.01 V increments, while the ln(I) values were experimentally measured and calculated.

The *ln(I)–V* curves of the Bi-GQDs/p-Si nanocomposite photodetector under dark and illumination conditions (22, 44, 66, 88, and 110 mW/mm^2), as shown in Fig. 3a, were directly recorded using the Keithley 4200 SCS, without any software modification other than standard plotting. The results reveal a clear correlation between light intensity and the device electrical response. The slight offset of the *ln(I)–V* curve at $V = 0$ V in the

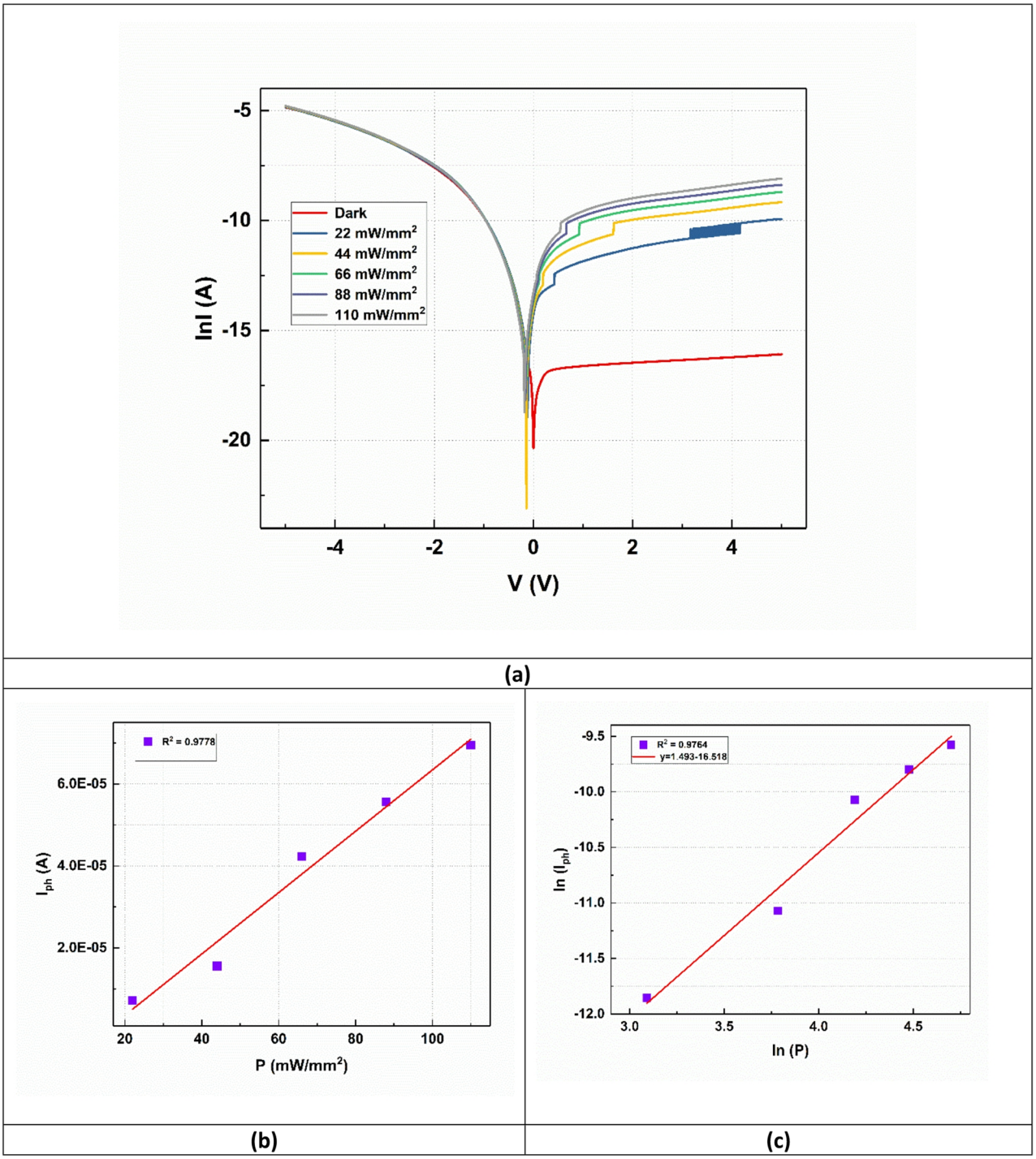


Fig. 3. (**a**) Semi-logarithmic *I*–*V* characteristics of the Bi-GQDs/p-Si nanocomposite photodetector measured under dark and various illumination power densities. (**b**) Photocurrent (I_{ph}) as a function of illumination power density (P (mW/mm^2)) at + 1 V bias. (**c**) The corresponding $ln(I_{ph})$–$ln(P)$ relationship fitted by the power-law equation $I_{ph} \propto P^{\gamma}$, yielding $\gamma = 1.49$.

dark is attributed to the built-in potential at the Bi-GQDs/p-Si interface, combined with contact resistance and measurement sensitivity effects. Under dark conditions, the device exhibits minimal current flow, with $ln(I)$ values decreasing sharply as the applied voltage increases. This behavior indicates low leakage current and confirms the high-quality rectifying nature of the device in the absence of illumination. From the $ln(I)$–V characteristics, the device exhibits a clear rectifying behavior, with a rectification ratio defined as $RR(V) = I(+V)/I(-V)$, yielding a value of 7.52×10^4 at 5 V under dark conditions. The low baseline current establishes a strong contrast against the illuminated conditions, which is crucial for evaluating photoresponse performance. As the illumination

Illumination intensity (P) 44 (mW/mm²)				
Model	**Output(*A*)**	***R²***	***MSE(A²)***	***MAE(A)***
AdaBoost	*ln(I)*	0.9599	0.2497	0.3634
GB	*ln(I)*	0.9049	0.5918	0.5454
XGBoost	*ln(I)*	0.9115	0.5507	0.5199
CatBoost	*ln(I)*	0.9124	0.5452	0.5184

Table 4. Statistical evaluation of the base ML models at an illumination intensity of 44 mW/mm². The table lists the predicted output variable (*ln (I)*), together with R^2, *MSE*, and *MAE* values for each model.

Illumination Intensity (P) 88 (mW/mm²)				
Model type	**Output (A)**	***R²***	***MSE(A²)***	***MAE(A)***
AdaBoost	*ln(I)*	0.9183	0.4273	0.5331
GB	*ln(I)*	0.9854	0.0761	0.1935
XGBoost	*ln(I)*	0.9870	0.0682	0.1840
CatBoost	*ln(I)*	0.9870	0.0682	0.1854

Table 5. Statistical evaluation of the base ML models at an illumination intensity of 88 mW/mm². The table lists the predicted output variable (*ln (I)*), together with R^2, *MSE*, and *MAE* values for each model.

intensity increases, the *ln(I)* values shift upward significantly across the voltage range. In particular, forward bias voltages result in a sharp increase in current, indicating efficient photogeneration of charge carriers. Each illumination level produces a distinct *ln(I)–V* curve, with higher light intensities leading to progressively higher current responses. The curve for 110 mW/mm² shows the most significant increase, followed by those at 88 mW/mm², 66 mW/mm², 44 mW/mm², and 22 mW/mm², respectively. This trend confirms that the device's performance is strongly dependent on illumination and that it demonstrates high photosensitivity across the examined range. A sharp dip in *ln(I)* values near 0 *V* is observed in all curves, consistent with the expected transition between reverse and forward bias regions in diode behavior. The results also confirm that the device maintains its rectifying behavior while exhibiting an enhanced, intensity-dependent photoresponse.

As shown in Fig. 3b, the photocurrent (I_{ph}) increases nonlinearly with illumination power density (*P*, mW/mm²) at + 1 V bias. The extracted exponent (γ = 1.49) from the $ln(I_{ph})$ –*ln(P)* fit (Fig. 3c) confirms a super-linear dependence, which can be attributed to trap-filling and photoconductive-gain effects in the Bi-GQDs/p-Si heterostructure[42].

These findings highlight the suitability of the Bi-GQDs/p-Si device for optoelectronic applications such as photodetectors or solar energy harvesting, where sensitivity and non-linearity are advantageous. Additionally, the well-separated response curves under different illumination levels provide a robust dataset for the development and evaluation of ML models aimed at modeling and predicting the diode's nonlinear photoresponse characteristics.

Table 4 summarizes the performance of four boosting basic models in predicting *ln(I)–V* characteristics at an illumination intensity of 44 mW/mm². Among the models, AdaBoost achieved the highest R^2 score of 0.9599, indicating strong linear correlation with the experimental data. It also recorded the lowest *MSE* (0.2497) and *MAE* (0.3634), outperforming the other models in all metrics at this illumination level. Although the gradient-based methods (GB, XGBoost, and CatBoost) produced comparable results, they demonstrated slightly higher error rates and lower R^2 values compared to AdaBoost. These findings suggest that AdaBoost, despite its relatively simple ensemble structure, was better suited to modeling the device's response under moderate illumination condition (44 mW/mm²), likely due to the less complex photocurrent behavior at this level.

Table 5 presents the performance of the same four boosting basic models under a higher illumination intensity of 88 mW/mm². Compared to the results at 44 mW/mm², all models—except AdaBoost—demonstrated significantly improved performance, with lower error values and higher R^2 scores. Notably, XGBoost, and CatBoost achieved the best overall results, recording the lowest *MSE* (0.0682), and *MAE* (0.1840 and 0.1854) respectively, along with an excellent R^2 value of 0.9874. GB and AdaBoost followed closely, showing almost identical metrics, highlighting their strong ability to generalize under increased illumination. This performance gap reinforces the idea that while AdaBoost may be adequate for moderate illumination levels, it struggles to capture the more complex and intensified nonlinear behavior at higher light intensities.

The overall reduction in error values for all models at 88 mW/mm² also confirms that the device's photoresponse becomes more consistent and predictable under stronger illumination, enabling ensemble basic learning algorithms to achieve greater accuracy. Among the tested models, AdaBoost yielded the most accurate prediction for detector performance at 44 mW/mm², whereas XGBoost, and CatBoost performed best under 88 mW/mm² illumination conditions.

To further improve predictive performance, four advanced boosting algorithms—AdaBoost, GB, XGBoost, and CatBoost—were trained individually. Their complementary strengths were then leveraged by employing a stacking ensemble technique, which combined their predictions to produce a more accurate and robust model. Table 6 presents the performance evaluation of the stacking ensemble model using statistical metrics. The

ensemble model shows strong predictive performance, especially under higher illumination. As the intensity increases from 44 to 88 mW/mm², the model's accuracy improves significantly — with R^2 rising to 0.9874 and error metrics (*MSE* and *MAE*) decreasing notably. This indicates that the ensemble approach effectively leverages the strengths of XGBoost and CatBoost, particularly under enhanced lighting conditions.

Figure 4a presents experimental and stacking ensemble predicted *ln(I)–V* curves at illumination intensities of 44 and 88 mW/mm². The results demonstrate a strong correlation between the predicted and experimental measurements, particularly in the forward bias region where the photocurrent increases rapidly. The stacking ensemble model successfully captures the overall shape and nonlinear behavior of the experimental curves. While the predicted curve at 44 mW/mm² aligns well with the experimental data, an even more accurate fit is observed at 88 mW/mm². This suggests that the model performs better at higher illumination intensities, likely due to more stable and pronounced photocurrent characteristics. These findings confirm the ensemble model's ability to generalize and interpolate between training conditions, further highlighting its effectiveness in predicting the device's behavior under previously unseen illumination levels. Figure 4b presents the statistical performance of the base models under two illumination intensities (44 and 88 mW/mm²), evaluated using R^2, *MSE*, *and MAE*. The plots were generated based on the predictions of the best-performing models: AdaBoost at 44 mW/mm² and XGBoost and CatBoost at 88 mW/mm². The R^2 values are high in both cases, with the model achieving near-perfect accuracy at 88 mW/mm². Both *MSE* and *MA*E significantly decrease as the illumination increases, indicating reduced prediction errors. The results show improved model accuracy and reduced errors at higher illumination levels. Figure 4c presents the performance of the stacking ensemble model, evaluated using three statistical metrics—R^2, *MSE*, and *MAE*—at two different illumination intensities (44 and 88 mW/mm²). At 44 mW/mm², the model shows relatively good performance with an R^2 above 0.9872; however, *MSE* and *MAE* values are notably higher compared to the results under stronger illumination. At 88 mW/mm², the ensemble model performs significantly better, achieving a near-perfect R^2 value (0.9874) and substantial reductions in both *MSE* and *MAE*. This highlights that the model benefits from increased illumination, leading to more accurate and reliable predictions. These findings align with the previously discussed *ln(I)–V* comparisons and further confirm that the model performs more accurately when photocurrent behavior is more stable and prominent—typically under stronger illumination. Therefore, the use of advanced ensemble models proves particularly effective in capturing complex optoelectronic behaviors in high-light conditions.

These predicted *ln(I)–V* characteristics enabled the extraction of illumination-dependent photodetector parameters. The key performance parameters of photodetectors are summarized as follows. Sensitivity ($S = \frac{I_{photo}}{I_{dark}}$) reflects the ability of the device to respond to weak optical signals and is often expressed as the minimum detectable input power or the output signal change per unit optical power. Responsivity ($R = \frac{I_{photo}-I_{dark}}{P_{inc}}$), defined as the ratio of the photocurrent to the incident optical power (P_{inc}), indicates the electrical output efficiency of the device. Specific detectivity (D^*) provides a noise-normalized figure of merit and is widely used to compare different detectors. It can be expressed as $D^* = \frac{\sqrt{A\Delta f}}{i_n}R$; where A is the device area, Δf the electrical bandwidth, and i_n the noise current. Table 7 shows the estimated photodetector parameters of Bi-GQDs/p-Si at 5 V, obtained using the stacking ensemble model's I-V characteristics. The photodetector exhibited notable performance across varying illumination intensities at 5 V. As shown in Table 7, under an illumination of 44 mW/mm², the device achieved a responsivity of 1.396 mA/W, and a specific detectivity of 6.79×10^9 Jones. When the illumination increased to 88 mW/mm², these values significantly improved to 2.389 mA/W, and 1.16×10^{10} Jones, respectively. These results indicate that the photodetector's response scales positively with increasing light intensity. The stacking ensemble model effectively captured the nonlinear relationship between illumination and photodetector response, enabling precise estimation of sensitivity and detectivity values.

Hybrid quantum dot (QD) photodetectors have demonstrated exceptional performance through synergistic material combinations. Konstantatos et al.[43] reported ultrahigh gain (~ 10^8 electrons per photon), responsivity of ~ 10^7 A·W^{-1}, and detectivity of 7×10^{13} Jones using graphene covered with colloidal QDs. Wang et al.[44] achieved a gain of ~ 10^9 and responsivity of ~ 6×10^5 A·W^{-1} in graphene–perovskite hybrids, while Subramanian et al.[45] demonstrated graphene QD/$CH_3NH_3PbI_3$ hybrids with responsivity of 12 A·W^{-1} and detectivity of 6.5×10^{11} Jones. More recently, Algadi et al.[5]fabricated N-doped GQDs/$CsPbBr_3$ heterostructures with responsivity of 0.24 A·W^{-1} and detectivity up to 2.5×10^{12} Jones. Parallel advances in QD–perovskite photodetectors have also been remarkable: Guo et al.[46,47] achieved responsivities up to 240 mA·W^{-1} and detectivities exceeding 10^{13} Jones using $CuInSe_2$ QDs with halide perovskites, Liu et al.[48] reported 521.7 mA·W^{-1} responsivity and 2.57×10^{12} Jones detectivity with SnS QDs in $FAPb_{0.5}Sn_{0.5}I_3$, and Kim et al.[49] demonstrated CdZnSeS/ZnS QD photodiodes with responsivity of 0.258 A·W^{-1} and detectivity of 1.0×10^{13} Jones. In comparison, our BiNPs&PEI-N-GQDs/p-Si photodetector exhibits responsivity values of 1.396–2.389 mA·W^{-1} and detectivity in the 10^9–10^{10} Jones range, which, while more modest than state-of-the-art perovskite–QD hybrids, surpass many graphene- and organic-

Model type	Illumination intensities (*P*) (mW/mm²)	R^2	MSE (A²)	MAE (A)
Ensemble (Stacked Generalization)	44	0.9872	0.0671	0.1812
	88	0.9874	0.0682	0.1840

Table 6. Statistical performance of the stacking ensemble model at illumination intensities of 44 and 88 mW/mm², showing excellent predictive accuracy with high R^2 and low *MSE* and *MAE* values.

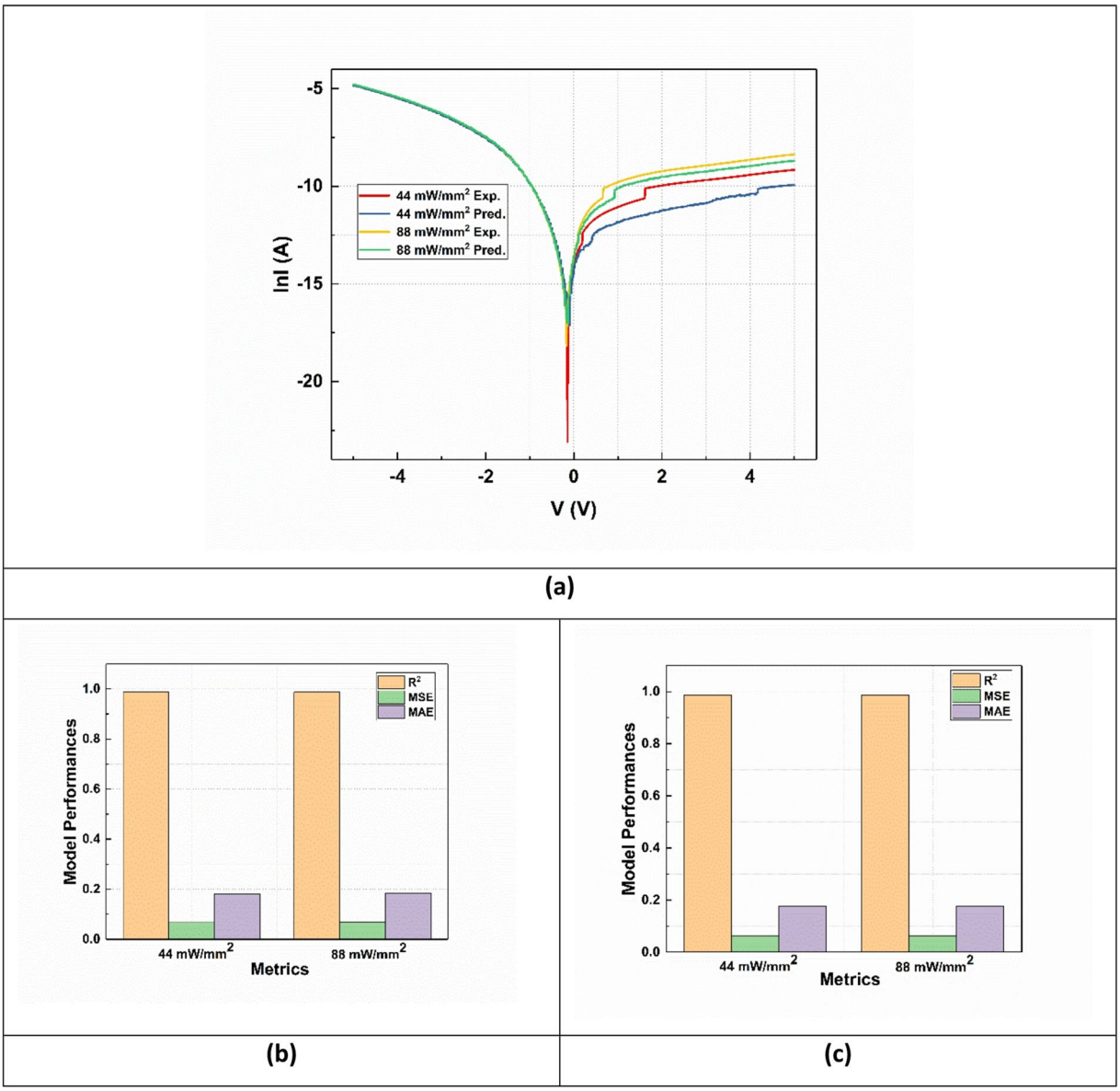


Fig. 4. (**a**) Comparison between the experimental and stacking-ensemble-predicted *ln(I)–V* characteristics of the Bi-GQDs/p-Si photodetector under illumination intensities of 44 mW/mm² and 88 mW/mm². (**b**) Statistical performance of the base models (AdaBoost, GB, XGBoost, and CatBoost) evaluated at different illumination levels using R^2, *MSE*, and *MAE* metrics. (**c**) Performance evaluation of the stacking ensemble model at 44 and 88 mW/mm², showing superior predictive accuracy with $R^2 > 0.98$ and minimal error values, confirming its robustness and generalization capability.

Model type	Illumination intensities (*P*) (mW/mm²)	Sensitivity (S)	Responsivity (*R*) (mA/W)	Specific detectivity* (D*) (Jones = cm.Hz$^{1/2}$W^{-1})
Ensemble (stacked generalization)	44	464.44	1.396	6.79×10^9
	88	1589.27	2.389	1.16×10^{10}

Table 7. Estimated photodetector performance parameters of the Bi-GQDs/p-Si device obtained from the stacking ensemble model's *I–V* characteristics. The table lists the sensitivity (*S*), responsivity (*R*), and specific detectivity (*D**) values calculated at illumination intensities of 44 mW/mm² and 88 mW/mm².

based devices. These results position our device as a stable, environmentally benign platform ideally suited for proof-of-concept machine learning modeling.

To provide a clear overview, Table 8 summarizes the key characteristics of the included studies. According to Table 8, all three studies employed supervised learning for photodetector modeling, using distinct model types: DTs[24], ensemble neural networks[29] and regression models[30]. Each study focused on a different photodetector type—2D metal halide perovskite, monolithic PET, and graphene-based FET, respectively—and reported varied performance metrics, including Root *MSE (RMSE)*, R^2, *MSE*, Full width at half maximum (FWHM), signal-to-noise ratio (SNR), contrast-to noise ratio (CNR), structural similarity index measure (SSIM). Similarly, Öter et al.[15] compared AI-driven and traditional approaches for predicting the behavior of polyethyleneimine-functionalized graphene quantum dot-based Schottky diodes. They applied four supervised learning algorithms—K-Nearest Neighbor, RF, MLPNN, and Support Vector Machine—to a dataset of 200 measurements from 30 physical diodes.

The performance of the included studies is evaluated through various prediction accuracy metrics, which are summarized in Table 9. According to Table 9, the studies employed distinct model types: DT -based models[24], ensemble neural networks[29] and polynomial regression[30]. Performance metrics varied across studies; Pandey et al.[24] reported low RMSE values for responsivity and detectivity, Iborra et al.[29] reported 2–2.4 mm FWHM and qualitative improvements in SNR, CNR, and SSIM without numerical values; Sorathiya et al.[30] cited R^2 and *MSE*, noting polynomial regression outperformed linear regression. Illumination conditions were specified only in Sorathiya et al.[30](deep UV); Pandey et al.[24] included irradiance as a model feature, while the third study did not report illumination details. Additionally, Öter et al.[15] applied for four supervised learning algorithms—including RF, which achieved a very low *MSE* of 4.1×10^{-5} and an R^2 of 0.999998—to model polyethyleneimine-functionalized GQDs-based Schottky diodes, although no illumination was applied in their experimental setup.

Conclusion

In this study, ensemble machine learning models—including AdaBoost, Gradient Boosting, XGBoost, and CatBoost—were successfully employed to predict the nonlinear photoresponse behavior of Bi-GQDs/p-Si photodetectors. The models were trained using datasets acquired under dark, 22 mW/mm², 66 mW/mm², and 110 mW/mm² illumination, and tested on intermediate levels (44 and 88 mW/mm²). The ensemble models accurately estimated the *ln(I)–V* characteristics and key performance metrics across 22–110 mW/mm², demonstrating robust predictive performance even at unseen illumination conditions. Responsivity and specific detectivity extracted from the stacking model's predictions reached 2.389 mA/W and 1.16×10^{10} Jones, respectively.

Study	Study objective/focus	ML method/approach	Photodetector type/material system	Remarks/target parameters
14	Analyzing the effects of varying temperatures on diode performance	KNN, DTs, and GB.	La doped GQDs based Schottky diode	-*ln(I)-V* characteristics, -R^2 -*MSE* -*MAE* -*MAPE*
15	AI-driven and traditional methods for predicting the characteristics of polyethyleneimine-functionalized GQDs based Schottky diodes.	KNN, RF, MLPNN, and Support Vector Machine.	Polyethyleneimine-functionalized nitrogen doped GQDs based Schottky diode	-*ln(I)-V* characteristics, -R^2 -*MSE*
24	Predicting responsivity and detectivity of two dimensional metal halide perovskite photodetectors using ML; model validation with experimental data	Six predictive models (including DT -based), and Supervised learning, no ensemble or hybrid approach mentioned.	Two dimensional metal halide perovskite photodetectors	-*RMSE* for responsivity and detectivity.
29	Three dimensional Position estimation in Monolithic PET detectors using Ensemble neural networks; validation with simulation and physical measurements	Ensemble of MLPNNs, Supervised learning, and Ensemble approach.	Monolithic positron emission tomography detectors	-*FWHM* -*SNR* -*CNR* -*SSIM*
30	Predicting photodetector responsivity (photocurrent) in graphene-based FETs operating in deep ultraviolet using supervised learning	Multiple linear regression, Polynomial regression, Supervised learning, and no ensemble or hybrid approach mentioned.	Graphene based photodetector (field-effect transistor, deep ultraviolet)	-R^2 -*MSE*
Present study	Analyzing the effects of varying illumination levels on detector performance using a stacking ensemble learning framework applied to Bi-GQDs/p-Si photodetectors.	-AdaBoost -GB -XGBoost -CatBoost -Stacking ensemble model	Bi-GQDs/p-Si photodetector	-*ln(I)-V* characteristics -R^2 -*MSE* -*MAE*

Table 8. Summary of previously reported ML studies related to photodetector modeling, including their objectives, ML approaches, device types, and target parameters. The table highlights how different algorithms—such as KNN, DT, GB, RF, and MLPNNs—have been applied to various photodetector architectures including La-doped GQDs, PEI-functionalized GQDs, perovskite, graphene-based, and PET detectors.

Study	Model type	Model/algorithm	Illumination conditions	Accuracy metrics	Key findings
[14]	Supervised machine Learning	KNN, DTs, GB	No illumination	R^2: 0.9999; *MSE*: 0.0027; *MAE*: 0.0195; *MAPE*: 0.1335	Very low MSE and MAE in GB model
[15]	Supervised machine Learning	RF	No illumination	R^2: 0.999998; *MSE*: 4.1×10^{-5}	Very low MSE under dark condition
[24]	DT	DT-based regression	Incident light intensity included as a feature	*RMSE*: 0.0092 (R), 0.0695 (D^*)	Very low RMSE for both training and validation
[29]	Ensemble neural Network (MLPNNs)	Ensemble of MLPNNs	Not specified; tested on 4 detectors	*FWHM*: 2–2.4 mm; *SNR*: 9.56 dB; *SSIM*: 0.849	Qualitative improvement in image metrics
[30]	Regression-based	Polynomial Regression	Deep UV illumination	R^2: 0.99; *MSE*: 0.0006091	Polynomial regression superior to linear regression
Present study	Ensemble ML (boosting + stacking)	AdaBoost, GB, XGBoost, CatBoost, Stacking	22–110 mW/mm²	AdaBoost (for 44 mW/mm²): -R^2:0.9599 -*MSE*:0.5918 -*MAE*:0.3634 XGBoost and CatBoost (for 88 mW/mm²) -R^2: 0.9872 and 0.9874 -*MSE*:0.0671 and 0.0682 -*MAE*:0.1812 and 0.1840 Ensemble-Stacked Generalization (for 44 mW/mm²): -R^2: 0.9872 -*MSE*:0.0671 -*MAE*:0.1812 Ensemble-Stacked Generalization (for 88 mW/mm²): -R^2: 0.9874 -*MSE*:0.0682 -MAE:0.1840	Consistently low error under multiple illumination levels, using a stacking ensemble approach applied to Bi-GQDs/p-Si photodetectors

Table 9. Comparison of prediction accuracy metrics and modeling approaches reported in related ML studies on photodetectors. The table summarizes the ML model types, algorithms, illumination conditions, evaluation metrics, and key outcomes of previous works.

To further enhance predictive capability, a stacking ensemble framework was implemented to integrate the strengths of the individual boosting models. The final stacking model showed strong performance in predicting *ln(I)–V* characteristics at 88 mW/mm², with an R^2 of 0.9874 and *MSE* of 0.0671. AI-based predictions enabled the estimation of responsivity, sensitivity, and detectivity without requiring extensive additional measurements, indicating the potential of data-driven approaches to support device analysis and reduce experimental workload. Future work may extend this methodology to other photonic devices or incorporate environmental variables to further improve prediction accuracy and broaden applicability.

Data availability

As part of our commitment to open science, the trained machine learning model files and all associated Python codes will be released as open-source to ensure transparency and reproducibility. The materials will be publicly available at [https://github.com/alioter71/](https://github.com/alioter71).

Received: 5 July 2025; Accepted: 19 December 2025
Published online: 13 January 2026

References

1. Orhan, E. et al. Effect of gadolinium on electrical properties of polyethyleneimine functionalized and Nitrogen-Doped graphene quantum Dot nanocomposite based diode. *Adv. Electron. Mater.* https://doi.org/10.1002/aelm.202300261 (2023).
2. Anter, A. et al. High-Frequency negative capacitance in graphene quantum Dots/Lanthanum (III) Hydroxide-based MIS heterostructure. *FlatChem* **49**, 100781 (2025).
3. Anter, A. et al. Lanthanum(III)hydroxide nanoparticles and Polyethyleneimine-Functionalized graphene quantum Dot nanocomposites in photosensitive silicon heterojunctions. *ACS Appl. Mater. Interfaces.* https://doi.org/10.1021/acsami.4c02102 (2024).
4. Chen, C. et al. Highly responsive MoS2 photodetectors enhanced by graphene quantum Dots. *Sci. Rep.* **5**, 11830 (2015).
5. Algadi, H. et al. Facile method for the Preparation of high-performance photodetectors with a GQDs/perovskite bilayer heterostructure. *Org. Electron.* **76**, 105444 (2020).
6. Kim, C. O. et al. High-performance graphene-quantum-dot photodetectors. *Sci. Rep.* **4**, 1–6 (2014).
7. Van Le, Q., Hong, K., Jang, H. W. & Kim, S. Y. Halide perovskite quantum Dots for light-emitting diodes: properties, synthesis, applications, and outlooks. *Adv. Electron. Mater.* **4**, 1800335 (2018).
8. Peighambardoust, N. S., Sadeghi, E. & Aydemir, U. Lead halide perovskite quantum Dots for photovoltaics and photocatalysis: a review. *ACS Appl. Nano Mater.* **5**, 14092–14132 (2022).
9. Kim, D., Yun, T., An, S. & Lee, C. L. How to improve the structural stabilities of halide perovskite quantum Dots: review of various strategies to enhance the structural stabilities of halide perovskite quantum Dots. *Nano Converg.* **11**, 4 (2024).
10. Dong, Y. et al. Recent advances toward practical use of halide perovskite nanocrystals. *J. Mater. Chem. Mater.* **6**, 21729–21746 (2018).
11. Leng, M., Chen, Z., Yang, Y., Zeng, K. & Tang, J. Synthesis and Optical Properties of Lead-Free Methylamine Bismuth Halide Perovskite Quantum dots, In: *Asia Communications and Photonics Conference*. AS1I-5 (Optica Publishing Group, 2016).

12. Leng, M. et al. All-inorganic bismuth-based perovskite quantum Dots with bright blue photoluminescence and excellent stability. *Adv. Funct. Mater.* **28**, 1704446 (2018).
13. Saddique, Z., Iqbal, Z. F., Imran, M., Latif, S. & Rasheed, T. Bismuth-based quantum Dots pioneering transformative breakthroughs in environment and energy sectors. *Mater. Today Commun.* **40**, 109431 (2024).
14. Ersöz, B. et al. Artificial intelligence-driven data generation for temperature-dependent current–voltage characteristics of diodes. *FlatChem* https://doi.org/10.1016/j.flatc.2025.100847 (2025).
15. Öter, A. et al. An artificial intelligence model Estimation for functionalized graphene quantum dot-based diode characteristics. *Phys. Scr.* **99**, 1–11. https://doi.org/10.1088/1402-4896/ad3515 (2024).
16. Dietterich, T. G. & Langley, P. Machine learning for cognitive networks: Technology assessment and research challenges. *Cognitive Networks: Towards Self-Aware Networks*. 97–120 (2007).
17. Ogutu, R. V. A., Rimiru, R. M. & Otieno, C. Target sentiment analysis ensemble for product review classification. *J. Inform. Technol. Res. (JITR)*. **15**, 1–13 (2022).
18. Zhang, Y., Liu, J. & Shen, W. A review of ensemble learning algorithms used in remote sensing applications. *Appl. Sci.* **12**, 8654 (2022).
19. Zhang, C. & Ma, Y. *Ensemble machine learning*. (Springer, 2012).
20. de Guia, J. D. et al. Application of ensemble learning with mean shift clustering for output profile classification and anomaly detection in energy production of grid-tied photovoltaic system, In: *2020 12th International Conference on Information Technology and Electrical Engineering (ICITEE)*. 286–291 (IEEE, 2020).
21. Yang, J. J. et al. Exploiting ensemble learning for automatic cataract detection and grading. *Comput. Methods Programs Biomed.* **124**, 45–57 (2016).
22. Kiran Rao, P., Giri Kumar, K., Bala Krishna, T. & Student pass percentage dedection using ensemble learninng., *Int. Res. J. Eng. Technol.* www.irjet.net (2020).
23. Simsek, E., Mahabadi, S. E. J., Carruthers, T. F. & Menyuk, C. R. Photodetector Performance Prediction with Machine Learning. In: F*rontiers in Optics*. FTu6C-4 (Optica Publishing Group, 2021).
24. Pandey, S. V. et al. A machine learning framework for predicting device performance in 2D metal halide perovskite photodetector. *Sol. Energy*. **270**, 112399 (2024).
25. Alfryyan, N. et al. Designing of near-IR organic semiconductors for photodetectors: machine learning and data mining assisted efficient pipeline. *Mater. Today Commun.* **36**, 106556 (2023).
26. Omer, Z. M. & Shareef, H. Adaptive boosting and bootstrapped aggregation based ensemble machine learning methods for photovoltaic systems output current prediction, In: *2019 29th Australasian Universities Power Engineering Conference (AUPEC)*. 1–6 (IEEE, 2019).
27. Omer, Z. M. & Shareef, H. Comparison of decision tree based ensemble methods for prediction of photovoltaic maximum current. *Energy Convers. Management: X*. **16**, 100333 (2022).
28. Simsek, E., Anjum, I. M., Carruthers, T. F. & Menyuk, C. R. Designing photodetectors with machine learning, In: *Novel Optical Materials and Applications, Optica Publishing Group*. NoW5C-2 (2022).
29. Iborra, A., González, A. J., Gonzalez-Montoro, A., Bousse, A. & Visvikis, D. Ensemble of neural networks for 3D position Estimation in monolithic PET detectors. *Phys. Med. Biol.* **64**, 195010 (2019).
30. Sorathiya, V., Kumar, M., Garai, B. & Saha, J. Prediction of Photodetector Response Using Supervised Learning, In: *2023 7th International Conference on Computation System and Information Technology for Sustainable Solutions (CSITSS)*. 1–6 (IEEE, 2023).
31. Yan, H. et al. *Manipulating infrared photons using plasmons in transparent graphene superlattices*. ArXiv Preprint https://ArXiv.org/abs/12025235 (2012).
32. Freitag, M. et al. Photocurrent in graphene Harnessed by tunable intrinsic plasmons. *Nat. Commun.* **4**, 1951 (2013).
33. Guo, J. et al. Type-printable photodetector arrays for multichannel meta-infrared imaging. *Nat. Commun.* **15**, 5193 (2024).
34. Guo, J. et al. Chromatic plasmonic polarizer-based synapse for all-optical convolutional neural network. *Nano Lett.* **23**, 9651–9656 (2023).
35. Mienye, I. D. & Sun, Y. A survey of ensemble learning: Concepts, algorithms, applications, and prospects. *Ieee Access.* **10**, 99129–99149 (2022).
36. Bentéjac, C., Csörgő, A. & Martínez-Muñoz, G. A comparative analysis of gradient boosting algorithms. *Artif. Intell. Rev.* **54**, 1937–1967 (2021).
37. Ferreira, A. J. & Figueiredo, M. A. T. Figueiredo, Boosting algorithms: A review of methods, theory, and applications. *Ensemble Mach. Learn. Methods Appl.* https://doi.org/10.1007/978-1-4419-9326-7_2 (2012).
38. Chen, T. & Guestrin, C. *Xgboost: A scalable tree boosting system, in: Proceedings of the 22nd Acm Sigkdd International Conference on Knowledge Discovery and Data Mining*. 785–794 (2016).
39. Hancock, J. T. & Khoshgoftaar, T. M. CatBoost for big data: an interdisciplinary review. *J. Big Data*. **7**, 94 (2020).
40. Mahajan, P., Uddin, S., Hajati, F. & Moni, M. A. Ensemble learning for disease prediction: a review. *Healthcare* **11**, 1808 (2023).
41. Divina, F., Gilson, A., Goméz-Vela, F., García Torres, M. & Torres, J. F. Stacking ensemble learning for short-term electricity consumption forecasting. *Energies (Basel)*. **11**, 949 (2018).
42. Vashishtha, P. et al. Epitaxial interface-driven photoresponse enhancement in monolayer WS2–MoS2 lateral heterostructures. *Adv. Funct. Mater.* https://doi.org/10.1002/adfm.202512962 (2025).
43. Konstantatos, G. et al. Hybrid graphene–quantum Dot phototransistors with ultrahigh gain. *Nat. Nanotechnol.* **7**, 363–368 (2012).
44. Wang, Y. et al. Hybrid graphene–perovskite phototransistors with ultrahigh responsivity and gain. *Adv. Opt. Mater.* **3**, 1389–1396 (2015).
45. Subramanian, A. et al. High-performance photodetector based on a graphene quantum dot/CH3NH3PbI3 perovskite hybrid. *ACS Appl. Electron. Mater.* **2**, 230–237 (2019).
46. Guo, R., Huang, F., Zheng, K., Pullerits, T. & Tian, J. CuInSe2 quantum Dots hybrid hole transfer layer for halide perovskite photodetectors. *ACS Appl. Mater. Interfaces*. **10**, 35656–35663 (2018).
47. Guo, R., Bao, C., Gao, F. & Tian, J. Double active layers constructed with halide perovskite and quantum Dots for broadband photodetection. *Adv. Opt. Mater.* **8**, 2000557 (2020).
48. Liu, Z. et al. Achieving high responsivity and detectivity in a quantum-dot-in-perovskite photodetector. *Nano Lett.* **23**, 1181–1188 (2023).
49. Kim, Y., Kim, J., Kim, H. & Jang, J. Quantum-dots photosensor with wide bandgap P-type and N-type oxide semiconductors for high detectivity and responsivity. *Adv. Mater. Technol.* **5**, 1900857 (2020).

Author contributions

Ş.S. and E.O. conceptualized the study and supervised the research. Z.B. performed the device fabrication and electrical characterization. A.Ö. and B.E. developed the machine learning models and contributed to the data analysis. All authors discussed the results, reviewed the manuscript, and approved the final version.

Declarations

Competing interests

The authors declare no competing interests.
The study does not report on or involve animal or human data or tissue use.

Additional information

Correspondence and requests for materials should be addressed to Ş.S. or E.O.

Reprints and permissions information is available at www.nature.com/reprints.

Publisher's note Springer Nature remains neutral with regard to jurisdictional claims in published maps and institutional affiliations.

Open Access This article is licensed under a Creative Commons Attribution-NonCommercial-NoDerivatives 4.0 International License, which permits any non-commercial use, sharing, distribution and reproduction in any medium or format, as long as you give appropriate credit to the original author(s) and the source, provide a link to the Creative Commons licence, and indicate if you modified the licensed material. You do not have permission under this licence to share adapted material derived from this article or parts of it. The images or other third party material in this article are included in the article's Creative Commons licence, unless indicated otherwise in a credit line to the material. If material is not included in the article's Creative Commons licence and your intended use is not permitted by statutory regulation or exceeds the permitted use, you will need to obtain permission directly from the copyright holder. To view a copy of this licence, visit http://creativecommons.org/licenses/by-nc-nd/4.0/.

© The Author(s) 2025